Research Article

An integrated design of novel RAFM steels with targeted microstructures and tensile properties using machine learning and CALPHAD

Xiaochen Li[1,2], Mingjie Zheng[1,3,*], Hao Pan[1,3,4] iD, Chunliang Mao[5], Wenyi Ding[1]

[1]Hefei Institutes of Physical Science, Chinese Academy of Sciences, Hefei 230031, Anhui, China.
[2]School of Physics and Electronic Engineering, Jining University, Qufu 273155, Shandong, China.
[3]University of Science and Technology of China, Hefei 230026, Anhui, China.
[4]Department of Mechanical Engineering, City University of Hong Kong, Hong Kong 999077, China.
[5]College of Mechanical Engineering, Yanshan University, Qinhuangdao 066004, Hebei, China.

[*]**Correspondence to:** Prof. Mingjie Zheng, Hefei Institutes of Physical Science, Chinese Academy of Sciences, 350 Shushanhu Road, Hefei 230031, Anhui, China. E-mail: mingjie.zheng@inest.cas.cn

Abstract

The design optimization of structure and performance of reduced activation ferritic-martensitic (RAFM) steels is crucial for the development of future fusion reactors, which has always been a significant challenge. In this study, we proposed a new strategy to integrate the microstructure and performance design of RAFM steels using machine learning (ML) and calculation of phase diagrams (CALPHAD). Since the microstructures (MX, $M_{23}C_6$, δ-ferrite, coarsening phases, *etc.*) play important roles in mechanical properties of RAFM steels, a microstructural model was built by ML to predict their volume fraction or presence based on the CALPHAD data. By integrating this microstructural model with the forward and reverse models, we developed two RAFM steels with high volume fraction of MX (0.49% and 0.42%) and excellent tensile properties. At 600 °C, the ultimate tensile strength (UTS) of the two RAFM steels is about 100 MPa higher than that of the conventional RAFM steels. These experimental results meet the specific design criteria, confirming the effectiveness of our design strategy. Our research will provide a valuable guideline for the design of other advanced alloys.

Keywords: Machine learning, integrated design, RAFM steels, tensile properties, MX precipitates

INTRODUCTION

Reduced activation ferritic-martensitic (RAFM) steels are derived from conventional 8-12 wt.% CrMoVNb ferritic-martensitic (FM) steels. To obtain low activation capability, the long-lived transmutation elements such as Mo, Nb and Ni in FM steels are replaced with short-lived transmutation elements such as W and Ta[1]. This modification is to simplify the waste management of highly radioactive components after their service in fusion reactors. The blanket system in fusion reactors requires materials that can withstand extreme conditions including high heat loads and exposure to high-energy (14 MeV) and high-fluence neutron irradiation[2]. With decades of development, RAFM steels have become promising candidate structural materials for blanket components of fusion reactors, because of their advantages in thermal mechanical properties, irradiation resistance, *etc.*[3-5]. The outstanding properties of RAFM steels are closely associated with their tempered ferritic/martensitic microstructure, comprising mainly martensitic laths and small precipitates such as $M_{23}C_6$ (M = Cr, W, Fe) and MX (M = V, Ta; X = C, N)[6,7]. However, the upper application temperature limit of conventional RAFM steels is ~550 °C[8-10], which restricts the operation of fusion reactors at higher temperatures and consequently limits the potential enhancement of power generation.

Conventional RAFM steels such as F82H and China low activation martensitic (CLAM) steel exhibit comparable tensile properties but poorer high-temperature creep resistance, compared with similar engineering FM steels such as Grade 91[11-14]. During the creep process of RAFM steels, the coarsening of martensitic laths, packets and blocks occurs, leading to material softening[15]. The microstructural evolution is mainly influenced by the coarsening of $M_{23}C_6$ and MX precipitates. The $M_{23}C_6$ precipitates at lath, block, packets and prior austenite grain boundaries (PAGBs) provide limited resistance to grain boundary migration during creep because of their easy coarsening to > 200 nm from initial ~100 nm[16,17]. In contrast, the nanoscale MX precipitates randomly distributed in the matrix exhibit good thermal stability, which acts as obstacles to pin dislocations during creep and decelerates the microstructure degradation[18,19]. Unfortunately, conventional RAFM steels contain only trace amounts of nanoscale MX precipitates. For example, the calculated volume fraction of MX precipitates (V_{MX}) in F82H is around 0.007%[20], significantly lower than the approximately 0.35% in Grade 91 steel[21]. Consequently, RAFM steels have lower creep resistance compared to engineering FM steels, which is mainly attributed to the significantly lower amount of MX precipitates.

In order to optimize V_{MX} in RAFM steels, researchers have mainly made great efforts to regulate the compositions and heat treatment conditions through two methods: trial-and-error experiment and calculation of phase diagrams (CALPHAD) modeling. For the former method, the focus is primarily on adjusting the content of elements (such as Ti, Ta, and Zr[22-25]). For example, the addition of 0.015 wt.% Ti increased the proportion of nano-sized TiC particles, resulting in a twofold improvement in creep-fatigue life of base RAFM steel[22]. Mao *et al.* enhanced 0.1C-RAFM by adding Ta and Zr elements, which promoted the precipitation of the MX phase[23]. This modification resulted in a nearly 100 MPa increase in ultimate tensile strength (UTS) at 600 °C and an approximately 1,900 h increase in creep rupture time at 600 °C/ 180 MPa. The study by Jun *et al.* indicated that a new RAFM steel with added Ta and Ti had a creep rupture time of 1,823 h under 550 °C/200 MPa condition, which is approximately three times that of EUROFER97 steel (592 h)[24]. This improvement is primarily attributed to the higher V_{MX} (0.12% *vs.* 0.0642%). However, the trial-and-error experiment faces challenges in optimizing multiple elements simultaneously, limiting further improvement of V_{MX}. For the latter method, it can compensate for the shortcomings of trial-and-error experiments in simultaneously optimizing multiple variables, thereby improving design efficiency. Klueh *et al.* proposed a CALPHAD-based outline for optimizing MX precipitates[26]. Following this approach, Tan *et al.* developed a variety of castable nanostructure alloys (CNAs) with high V_{MX} (> 0.4%) by

optimizing the compositions and heat treatment conditions[21,27]. After testing, it was found that the tensile properties and creep resistance of CNAs were greatly improved compared with EUROFER 97. Although CALPHAD can predict microstructures from compositions and heat treatment parameters, it struggles to establish quantitative relationships with properties, hindering efficient material design.

In recent years, machine learning (ML) method has been applied to discover advanced materials. The core of this method lies in developing prediction models describing the relationships between compositions, processing parameters, microstructures, and properties[28]. Once accurate prediction models are established, the properties of thousands of candidate materials can be efficiently calculated, guiding subsequent experimental testing. For example, Wen *et al.* developed a ML-based hardness prediction model to accelerate the discovery of Al-Co-Cr-Cu-Fe-Ni alloys with enhanced hardness[29]. Similarly, Yu *et al.* proposed a new design strategy to screen Co-base superalloys with excellent properties from 363,000 candidates using four ML-based prediction models[30]. However, most ML studies mainly focus on performance optimization, as limited experimental data poses challenges to developing accurate microstructural models. Moreover, there are few reports on ML-based design of RAFM steels, aside from the study by Wang *et al.* and our recent work[31,32]. A ML model was developed by Wang *et al.* to predict the tensile properties of RAFM steels based on their compositions and heat treatments[31]. In our recent work[32], we introduced a ML-based intelligent design model to guide the compositional and processing design of RAFM steels. This model facilitated the development of a new RAFM steel achieving a UTS ~100-400 MPa higher than that of conventional RAFM steels, with comparable total elongation (TE). Unfortunately, its calculated V_{MX} of ~0.03% is significantly lower than that of FM steels (such as ~0.35% in Grade 91[21]). If the prediction problem of microstructures in this intelligent design model can be solved, it will help to quickly discover RAFM steels with high V_{MX} and excellent tensile properties.

In this work, a combination of CALPHAD and ML has been naturally proposed to achieve the integrated design of structure and performance. Firstly, accurate microstructural dataset was provided by high-throughput CALPHAD to support ML modeling. Based on this dataset, a microstructural model is constructed, taking compositions and heat treatments as inputs and microstructural attributes as outputs. Secondly, an integrated design model is built by combining the microstructural model with the forward and reverse models from our former work[32], executing the structure-property-oriented compositional and processing design. Finally, this model is employed to develop new RAFM steels with desired microstructures and tensile properties, followed by necessary experimental validations.

MATERIALS AND METHODS
Design strategy
An accelerated design strategy, incorporating ML and CALPHAD, was applied to develop new RAFM steels with targeted microstructures and tensile properties, as shown in Figure 1. The process involves the following steps:

First, three data-driven prediction models were established: a forward model, a reverse model, and a microstructural model. The forward model predicts the tensile properties of RAFM steels based on their compositions and processing parameters, while the reverse model suggests candidate combinations of compositions and processing parameters to achieve targeted tensile properties. The forward and reverse models with high accuracy were developed and validated in our previous work[32]. The microstructural model includes four sub-models to predict: (1) the presence of δ-ferrite at normalizing temperature (NT); (2) the presence of coarsening phases (i.e., Laves and Z-phase) at tempering temperature (TT); (3) the volume fraction of MX (V_{MX}) at TT; and (4) the volume fraction of $M_{23}C_6$ precipitates (V_{M23C6}) at TT.
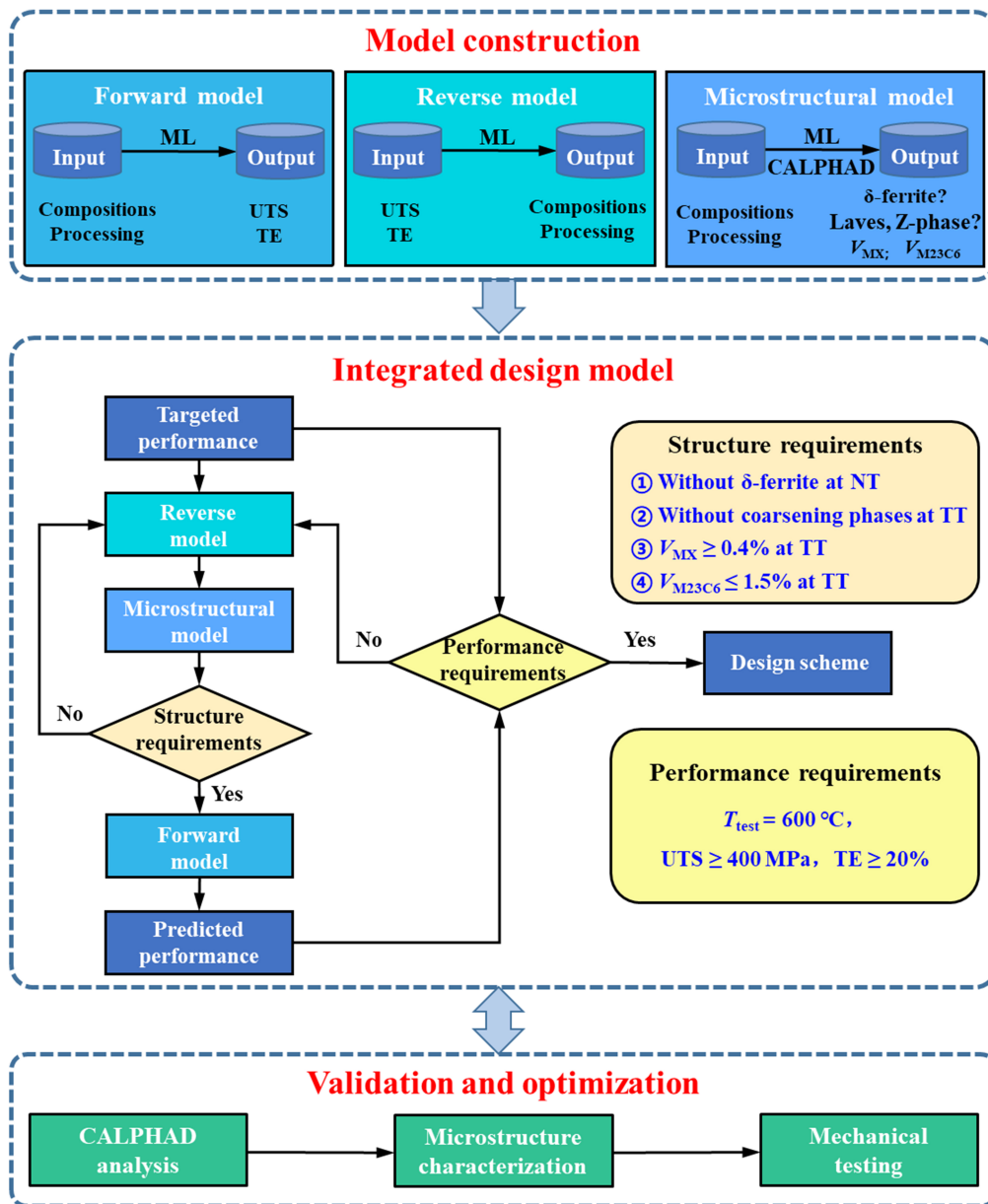
Figure 1. The designing process of novel RAFM steels with targeted microstructures and tensile properties. RAFM: Reduced activation ferritic-martensitic.

Second, the forward, reverse, and microstructural models are combined to form an integrated design model. The reverse model takes targeted performance metrics as inputs to propose an initial design scheme for compositions and processing. The microstructural model then predicts the microstructural attributes of the aforementioned design scheme. If the predicted microstructures meet the requirements, the design scheme is accepted. If not, the reverse model is retrained, and the process is repeated until a suitable design scheme is found. The forward model then predicts the performance of the accepted design scheme, which is compared to the targeted performance. If the performance criteria are not met, retraining and iterations continue until a satisfactory design scheme is founded.

Finally, the selected design scheme undergoes validation through the CALPHAD and experimental methods. If the new RAFM steel meets all design criteria, the process is complete. If not, the testing data are added to the training dataset for the next iteration.

Data preparation

The dataset used in this study regarding the tensile properties of RAFM steels was from our former work[32]. For the microstructural dataset, it was collected from phase diagrams calculated by the Thermo-Calc software with the TCFE10 database[33]. Firstly, compositions and heat treatment parameters of RAFM steels were collected from literature, and used as inputs for CALPHAD predictions. To ensure low activation and reflect the typical compositions of RAFM steels, the following alloying elements were chosen: C, Cr, W, Si, Mn, V, Ta, Ti, and N. The heat treatment parameters (NT; Nt: normalizing time; TT; Tt: tempering time) were chosen based on commonly reported preparation conditions of RAFM steels, ensuring the representativeness and reliability of the data. Secondly, CALPHAD step diagrams were digitized to obtain the microstructural data for δ-ferrite, coarsening phases (i.e., Laves and Z-phase), V_{MX}, and V_{M23C6} under different heat treatment parameters. Finally, the microstructural dataset included 209 samples with δ-ferrite and 202 samples without (named Data-I); 76 samples with coarsening phases and 144 samples without (named Data-II); 219 samples for V_{MX} (named Data-III); 219 samples for V_{M23C6} (named Data-IV). The data distribution of the microstructural dataset is provided in Supplementary Figure 1. To reduce dimensional differences and improve calculation accuracy, it was necessary to normalize the collected datasets to [0, 1].

ML algorithms

In this study, various ML algorithms were chosen to build prediction models, including decision tree, random forest, support vector machine, gradient boosting, k-nearest neighbor, and artificial neural network. The unique characteristics of each algorithm are outlined in the Supplementary Section 2. The decision tree classifier (DTC), random forest classifier (RFC), support vector classifier (SVC), gradient boosting classifier (GBC), k-nearest neighbor classifier (KNC), and artificial neural network classifier (ANNC) were used to build the classification models. The effectiveness of these classification models was assessed based on their accuracy (*Acc*), which is calculated by[34,35]

$$Acc = \frac{T}{T+F} \times 100\% \tag{1}$$

where T represents the number of correct classifications, and F denotes the number of incorrect classifications. An *Acc* of 100% indicates perfect model fitting. This study also applied several common ML regression algorithms, including decision tree regression (DTR), random forest regression (RFR), support vector regression (SVR), gradient boosting regression (GBR), k-nearest neighbor regression (KNR), and artificial neural network regression (ANNR). The performance of these regression algorithms was evaluated using the root mean square error (RMSE) and the coefficient of determination (R^2), defined as follows[36,37]:

$$\text{RMSE} = \sqrt{\frac{1}{n}\sum_{i=1}^{n}(y_i - \hat{y}_i)^2} \tag{2}$$

$$R^2 = 1 - \frac{\sum_{i=1}^{n}(y_i - \hat{y}_i)^2}{\sum_{i=1}^{n}(y_i - \bar{y})^2} \tag{3}$$

where n is the number of samples; y_i and $\hat{y}_i$ represent the measured and predicted values of the i-th sample (i = 1, 2, ..., n), respectively; and $\bar{y}$ is the mean of the measured values. In theory, a perfectly accurate model would have an RMSE of 0 and an R^2 of 1. The predictive performance of these models was evaluated using the hold-out method. The 80% of the normalized dataset was used for training, and the remaining 20% was utilized to assess model errors. According to a pedagogical analysis by Gholamy *et al.*, this 80:20 split was determined to be the optimal division between training and testing datasets[38].

Experimental procedures
According to the designed compositions in Table 1, two 10 kg ingots were produced by vacuum induction melting. The ingots were homogenized at 1,200 °C for two hours before being processed through hot forging and hot rolling to a thickness of 16 mm. Subsequently, according to heat treatment parameters listed in Table 1, two 16-mm thick plates were normalized and tempered followed by air cooling. The microstructural features of the RAFM steels were analyzed through scanning electron microscopy (SEM) and transmission electron microscopy (TEM). For SEM characterization, the samples were etched with a mixed solution (2% hydrofluoric acid + 2% nitric acid + 96% de-ionized water) after mechanical polishing. TEM samples were prepared by mechanical polishing followed by twin-jet polishing in a solution of 90% ethanol and 10% perchloric acid at 20 V and -35 °C. To ensure reliable dislocation density measurements, the line intersection method described in Refs.[39,40] was applied to at least three different TEM micrographs. For non-spherical MX and $M_{23}C_6$ particles, two perpendicular axes (a and b) were measured by Image J software based on more than ten TEM micrographs, and their average diameter (d) was calculated as (a + b)/2. The volume fraction (V) of MX and $M_{23}C_6$ was estimated by

$$V = \frac{\sum_{i=1}^{m} \frac{4}{3}\pi\left(\frac{d_i}{2}\right)^3}{\sum_{j=1}^{n} A_j t} \tag{4}$$

where m represents the number of precipitates in n TEM micrographs; d_i is the diameter of the i-th precipitate (i = 1, 2, ..., m); A_j denotes the area of the j-th TEM micrograph (j = 1, 2, ..., n); t is TEM sample thickness with a value of 200 nm[40]. Specimens with dimensions of 4 × 20.0 mm, extracted from the plates in the rolling direction, were subjected to tensile tests at 25, 300, 400, 500, and 600 °C. The tests were conducted at a crosshead speed of 2 mm/min, resulting in a strain rate of around 1.67 × 10^{-3} s^{-1}.

RESULTS AND DISCUSSION

Model construction
The forward, reverse, and microstructural models each play specific roles in achieving the integrated design of novel RAFM steels with targeted microstructures and tensile properties. The reverse model proposes candidate design schemes of compositions and processing parameters based on targeted performance metrics. The microstructural and forward models predict the essential microstructures and tensile properties of these candidate designs, which are then compared to the targeted requirements. Through an iterative process of feedback, validation, and optimization, novel RAFM steels are developed to meet the specific structure and performance criteria. The following provides a detailed description of the construction results of the forward, reverse, and microstructural models.

Forward and reverse models
The forward model with high reliability was constructed by the GBR algorithm to predict the tensile properties of RAFM steels. For the reverse model, it was built by the ANNR algorithm to generate candidate compositions and processing parameters for targeted tensile properties. These two models have been

Table 1. Compositions and processing conditions designed by an integrated design model based on specific requirements

No.	Compositions (wt.%)									Processing parameters			
	C	Cr	W	Si	Mn	V	Ta	Ti	N	NT (°C)	Nt (min)	TT (°C)	Tt (min)
1#	0.140	8.64	1.30	0.30	0.57	0.320	0.180	0.200	0.0003	1120	21	720	62
2#	0.055	8.40	0.26	0.15	0.50	0.314	0.167	0.217	0.0030	1020	30	650	50

NT: Normalizing temperature; Nt: normalizing time; TT: tempering temperature; Tt: tempering time.

developed in our previous work[32] and can be directly used in this study.

Microstructural model

The ideal microstructures of RAFM steels should avoid the presence of δ-ferrite, Laves, and Z-phase. δ-ferrite is regarded as an easy propagation site for intragranular cleavage fractures[41]. The coarsening of Laves phase significantly weakens microstructural stability and accelerates void growth[42,43], adversely affecting the mechanical properties of RAFM steels. The coarsening of Z-phase consumes fine MX-type precipitates during long-term testing and servicing, impairing the strength of RAFM steels[21]. In this section, the ML classification algorithms were applied to construct prediction models for identifying the presence of δ-ferrite at NT (named as Model-I) and the presence of coarsening phases (i.e., Laves and Z-phase) at TT (named as Model-II). For Model-I, the inputs were compositions and NT, while Model-II used compositions and TT as inputs.

Figure 2A displays the predictive performance of Model-I constructed by six common ML classification algorithms, with each data point averaged over 100 learning processes to reduce random error. It can be learned from Figure 2A that the Model-I model developed by the GBC algorithm achieves the highest *Acc* value among the selected six ML algorithms. Figure 2B shows the predictive ability of Model-II constructed by six ML classification algorithms based on Data-II dataset. Similar to the results in Figure 2A, Model-II constructed by the GBC algorithm has the highest *Acc* among the selected six ML algorithms, indicating its best predictive ability. Based on Data-I dataset, Model-I was constructed by GBC algorithm and its detailed classification results are shown in confusion matrix of Figure 2C. In the training sets, Model-I achieves the *Acc* of 100% in identifying both "with δ-ferrite" and "without δ-ferrite" classes. For the testing sets, Model-I classifies "with δ-ferrite" and "without δ-ferrite" with *Acc* of 100% and 98.0%, respectively. Model-I exhibits high accuracy (> 90%), indicating that it has excellent predictive ability for identifying the presence of δ-ferrite at NT and neither obvious overfitting nor under-fitting issues. The confusion matrix in Figure 2D shows the detailed classification results of Model-II. As shown in Figure 2D, Model-II constructed by the GBC algorithm achieves the *Acc* of > 85.0% in both the training and testing sets. The above analysis results demonstrate that the Model-I and Model-II constructed in this work have good robustness and reliability.
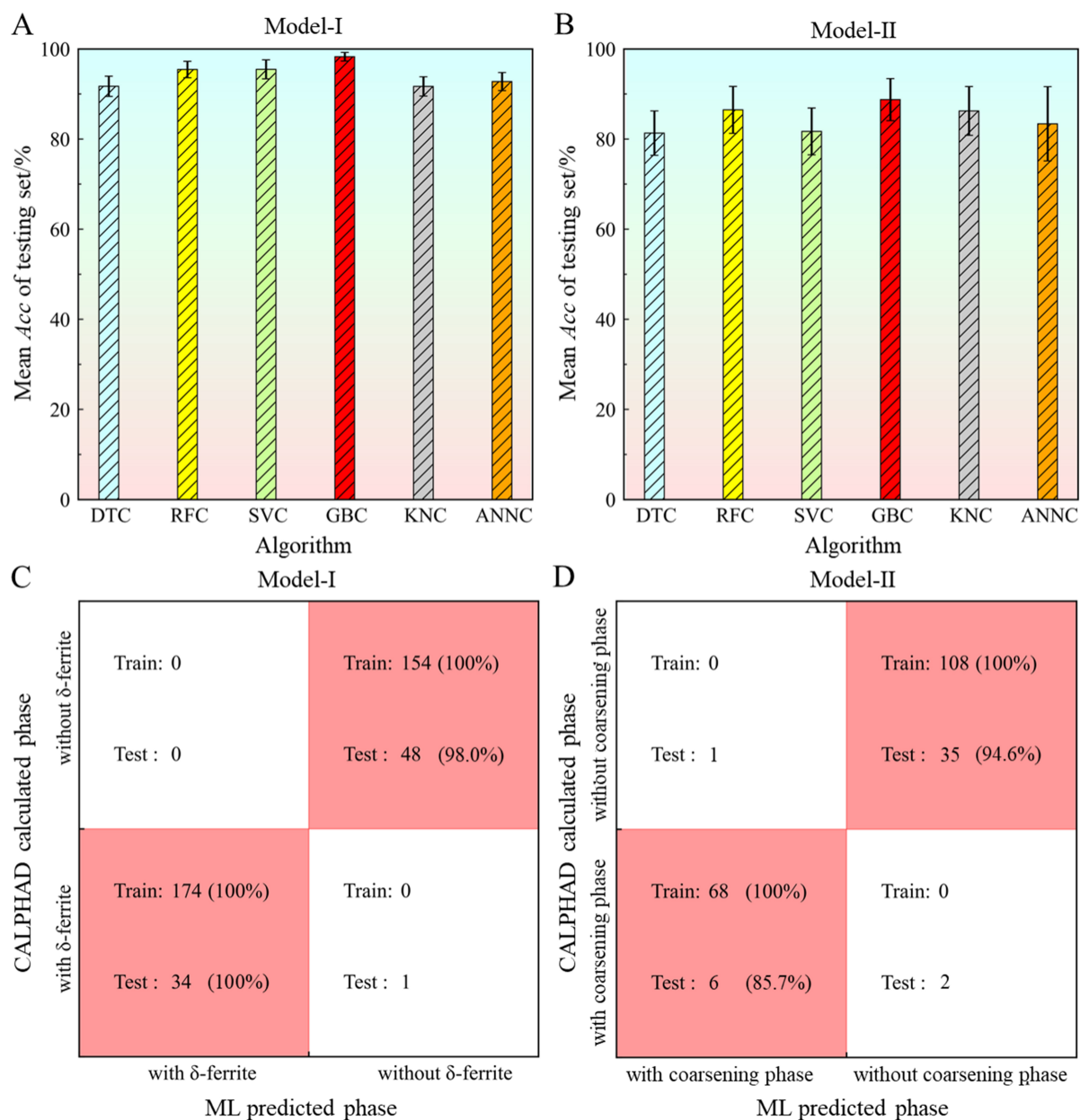
Figure 2. The mean *Acc* values of the (A) Model-I and (B) Model-II models constructed by the DTC, RFC, SVC, GBC, KNC, and ANNC algorithms; the confusion matrixes of the (C) Model-I and (D) Model-II models constructed by the GBC algorithm. DTC: Decision tree classifier; RFC: random forest classifier; SVC: support vector classifier; GBC: gradient boosting classifier; KNC: k-nearest neighbor classifier; ANNC: artificial neural network classifier.

The V_{MX} and V_{M23C6} are two crucial microstructural attributes affecting the mechanical properties of RAFM steels and need to be appropriately controlled. In this section, different ML regression algorithms were applied to construct Model-III and Model-IV for predicting V_{MX} and V_{M23C6}, respectively. The compositions and TT were set as inputs for Model-III and Model-IV.

Each ML algorithm has its own advantages when dealing with different types of datasets. In order to select the appropriate algorithm, Model-III was constructed by six ML regression algorithms (DTR, RFR, SVR,

GBR, KNR, and ANNR), and its predictive abilities were assessed through the hold-out method. The RMSE and R^2 values of Model-III constructed by these algorithms are illustrated in Figure 3A. To reduce random error, the RMSE and R^2 values for each algorithm were averaged over the results of 100 learning processes. As shown in Figure 3A, the RFR algorithm exhibits the smallest RMSE value and the largest R^2 value among the six ML algorithms, indicating the best fitting effect. Therefore, the RFR algorithm was chosen to construct the Model-III for predicting V_{MX}. Similarly, for the Model-IV model, the average RMSE and R^2 values of six ML regression algorithms are summarized in Figure 3B. It is clear that compared to the other four algorithms, the SVR and GBR algorithms exhibit better predictive ability because of their smaller RMSE and larger R^2. Further analysis reveals that although the average RMSE value of the SVR algorithm is higher than that of the GBR algorithm, its standard deviation value is smaller. Moreover, the SVR algorithm exhibits a higher R^2 value and a smaller standard deviation value compared to the GBR algorithm. From the perspective of standard deviation value, a smaller value indicates greater model stability. From the above analyses, the SVR algorithm was selected to build Model-IV for predicting V_{M23C6}. Figure 3C presents the comparison of V_{MX} values predicted by Model-III and calculated by the CLAPHAD method. The majority of data points are located near the diagonal (marked by the red dotted line in Figure 3C), with R^2 values of > 0.9 for both training and testing sets. An R^2 value of > 0.8 indicates a strong correlation, with the predicted values closely matching the observed values[44]. This clearly shows that Model-III constructed by the RFR algorithm has high predictive ability for V_{MX}. Figure 3D plots the V_{M23C6} values predicted by Model-IV against those calculated by the CALPHAD method. Model-IV demonstrates strong predictive performance in both the training and testing sets with an $R^2 > 0.9$, comparable to the performance of Model-III. A good agreement between the predicted and the calculated results is also illustrated by the scatter points distributed closely to the red diagonal. The above analysis results support a reasonable conclusion that the prediction models constructed for the four crucial microstructural attributes of RAFM steels exhibit good accuracy and reliability. These four sub-models (i.e., Model-I, Model-II, Model-III, and Model-IV) are integrated together to form a microstructural model used for designing novel RAFM steels.

Design of novel RAFM steels

To achieve the design of RAFM steels with targeted microstructures and tensile properties, the forward and reverse models as well as the microstructural model were coupled together to construct an integrated design model, as shown in Figure 1. In this section, the effectiveness of the integrated design model is demonstrated by designing novel RAFM steels satisfying specific structure and performance requirements. It is crucial to avoid δ-ferrite, Laves, and Z-phase in RAFM steels as they are harmful for high-temperature mechanical properties. MX precipitates exhibit excellent thermal stability, whereas $M_{23}C_6$ precipitates are prone to coarsening at high temperatures. Consequently, enhancing the strength and creep resistance may be achieved by increasing V_{MX} while reducing V_{M23C6}. In this study, the targeted V_{MX} and V_{M23C6} are set higher and lower than the typical levels of < 0.2% and ~2%, respectively, found in conventional RAFM steels[21]. The newly designed RAFM steels are expected to exhibit a higher UTS value at 600 °C compared to conventional RAFM steels, while maintaining a similar TE. The specific requirements are summarized as follows:

i. without δ-ferrite at NT;
ii. without Laves and Z-phase at TT;
iii. $V_{MX} \geq 0.4\%$ at TT;
iv. $V_{M23C6} \leq 1.5\%$ at TT;
v. test temperature (T_{test}) = 600 °C, UTS ≥ 400 MPa, TE ≥ 20%.

Considering the particularity of this study, the performance requirements do not need to have a deviation of < 10% between the predicted and targeted tensile properties, as was the case in our former work[32]. One of the biggest differences between this study and our previous work[32] is the addition of structure
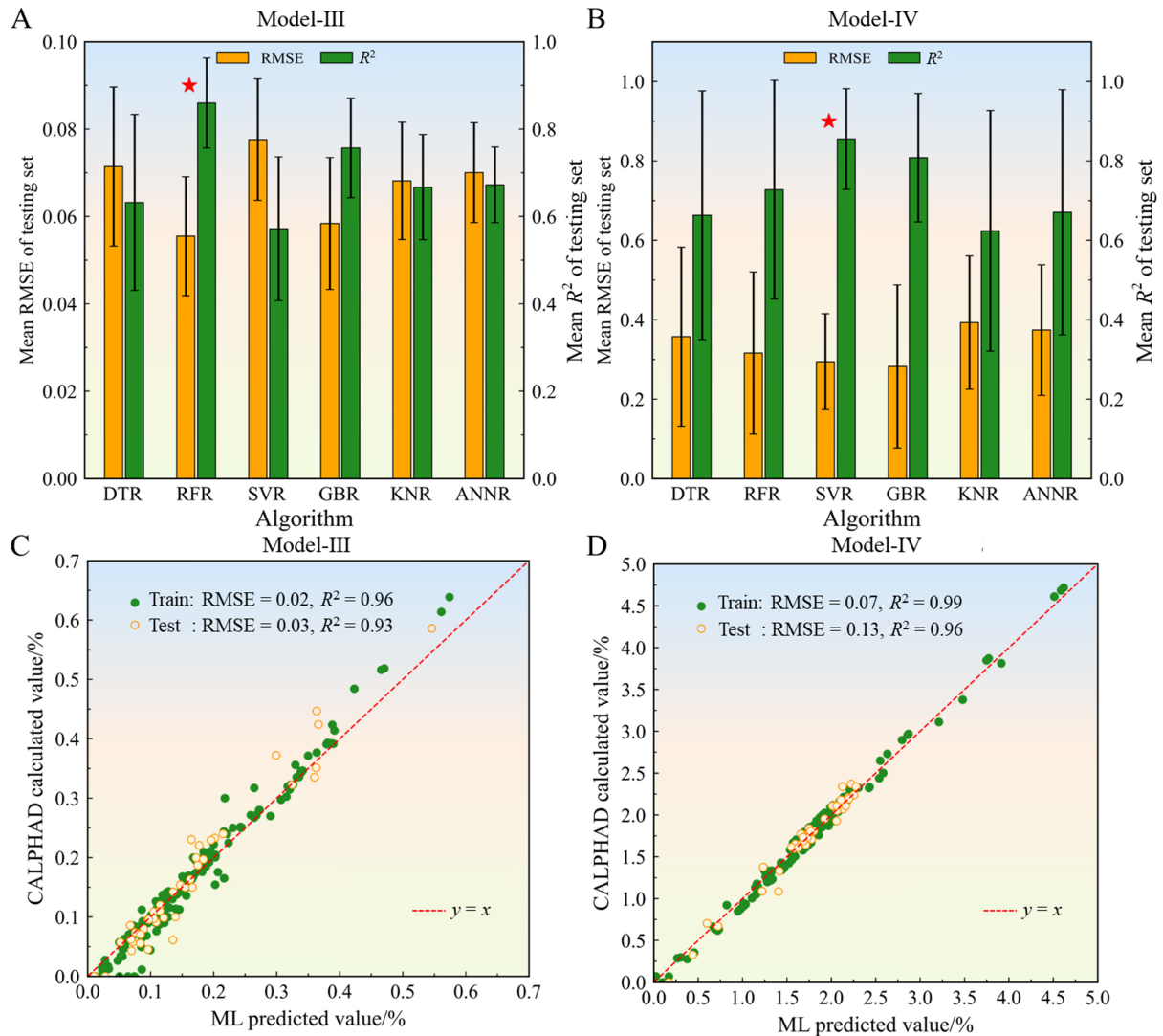
Figure 3. The mean RMSE and R^2 values of (A) Model-III and (B) Model-IV constructed by DTR, RFR, SVR, GBR, KNR, and ANNR algorithms; the comparison of the predicted values by (C) Model-III and (D) Model-IV models and calculated values by CALPHAD. RMSE: Root mean square error; DTR: decision tree regression; RFR: random forest regression; SVR: support vector regression; GBR: gradient boosting regression; KNR: k-nearest neighbor regression; ANNR: artificial neural network regression; CALPHAD: calculation of phase diagrams.

requirements. It is very challenging to control the predicted performance of the proposed design scheme within a defined range while meeting the structure requirements.

Using the targeted performance criteria (T_{test} of 600 °C, UTS of 400 MPa, and TE of 20%) as inputs, the integrated design model was run to design novel RAFM steels meeting both structure and performance requirements. Table 1 lists two representative compositional and processing schemes, with the corresponding CALPHAD results presented in Figure 4. Table 2 summarizes the microstructural attributes of the aforementioned two design schemes calculated by the ML and CALPHAD methods. For 1# and 2# steels, the ML prediction results show no δ-ferrite or large-size coarsening phases (i.e., Laves and Z-phase), which is well consistent with the CALPHAD calculations. The ML-predicted V_{MX} and V_{M23C6} of 1# steel are 0.52% and 1.41%, respectively, which are very close to the CALPHAD-calculated values of 0.60% and 1.30%.

Table 2. The microstructural attributes and tensile properties of two designed RAFM steels in Table 1

No.	Methods	Microstructures		V_{MX} (%)	V_{M23C6} (%)	Tensile properties at 600 °C	
		δ-ferrite	Coarsening phase			UTS (MPa)	TE (%)
1#	ML	Without	Without	0.52	1.41	412	21.5
	CALPHAD			0.60	1.30	-	-
	Experiment			0.49	1.38	404	21.0
2#	ML	Without	Without	0.48	-	445	20.2
	CALPHAD			0.50	-	-	-
	Experiment			0.42	-	422	19.3

RAFM: Reduced activation ferritic-martensitic; UTS: ultimate tensile strength; TE: total elongation; ML: machine learning; CALPHAD: calculation of phase diagrams.
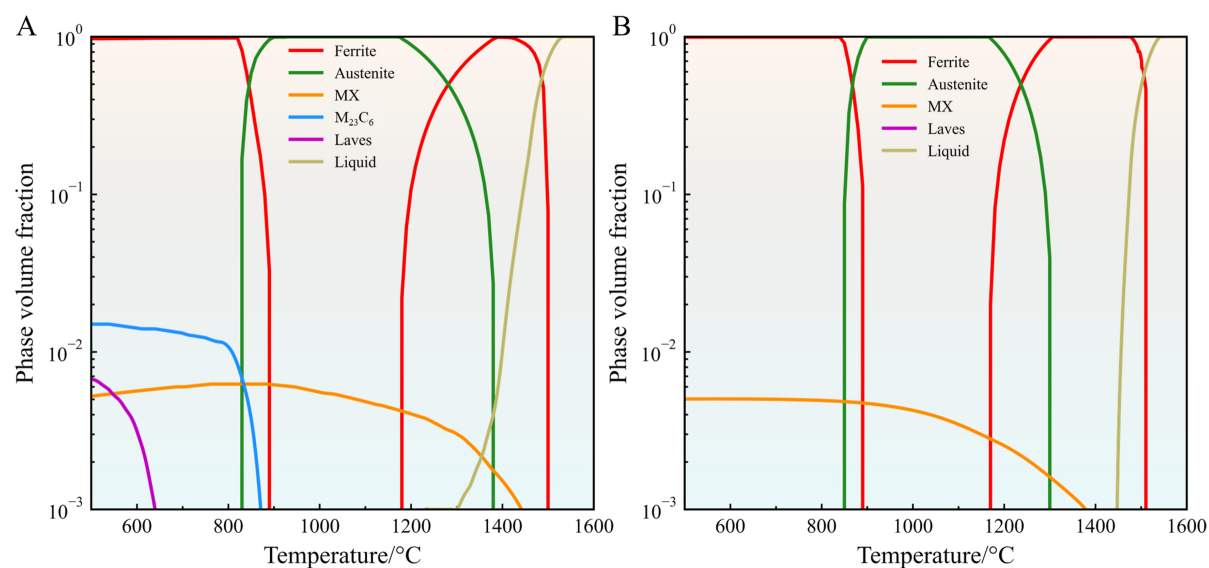

Figure 4. The equilibrium volume fraction of phases at different temperatures calculated by the Thermo-Calc software: (A) 1# steel and (B) 2# steel.

Similarly, the V_{MX} of 2# steel predicted by ML is nearly identical to that calculated by CALPHAD (0.48% *vs.* 0.50%). These analyses indicate that the ML predictions are in good agreement with the CALPHAD calculations, and the microstructural model constructed in this study exhibits strong predictive ability.

Experimental validation

To further verify the practical effectiveness of the design schemes proposed by the integrated design model, 1# and 2# steels listed in Table 1 were prepared and characterized. Figure 5 shows the SEM images of the newly designed 1# and 2# steels. It can be seen from Figure 5A(1) that the 1# steel is a fully martensitic structure without δ-ferrite, Laves, and Z-phase. Similarly, the 2# steel has a low-carbon martensitic structure without these phases, as shown in Figure 5A(2). Using the standard linear intercept method, the mean prior austenite grain sizes of 1# and 2# steels are measured to be 18.8 and 9.7 m, respectively. The micrograph of 1# steel in Figure 5B(1) reveals that the PAGB and lath boundary (LB) are decorated with $M_{23}C_6$ and MX precipitates, as observed in other RAFM steels[45,46]. However, it is difficult to find $M_{23}C_6$ carbides distributed along PAGB and LB in 2# steel, as illustrated in Figure 5B(2). Some MX precipitates distributed in the matrix can be clearly observed in 2# steel. The above SEM analyses confirm that both 1# and 2# steels exhibit a fully martensitic structure without δ-ferrite, Laves, and Z-phase, which is consistent with the
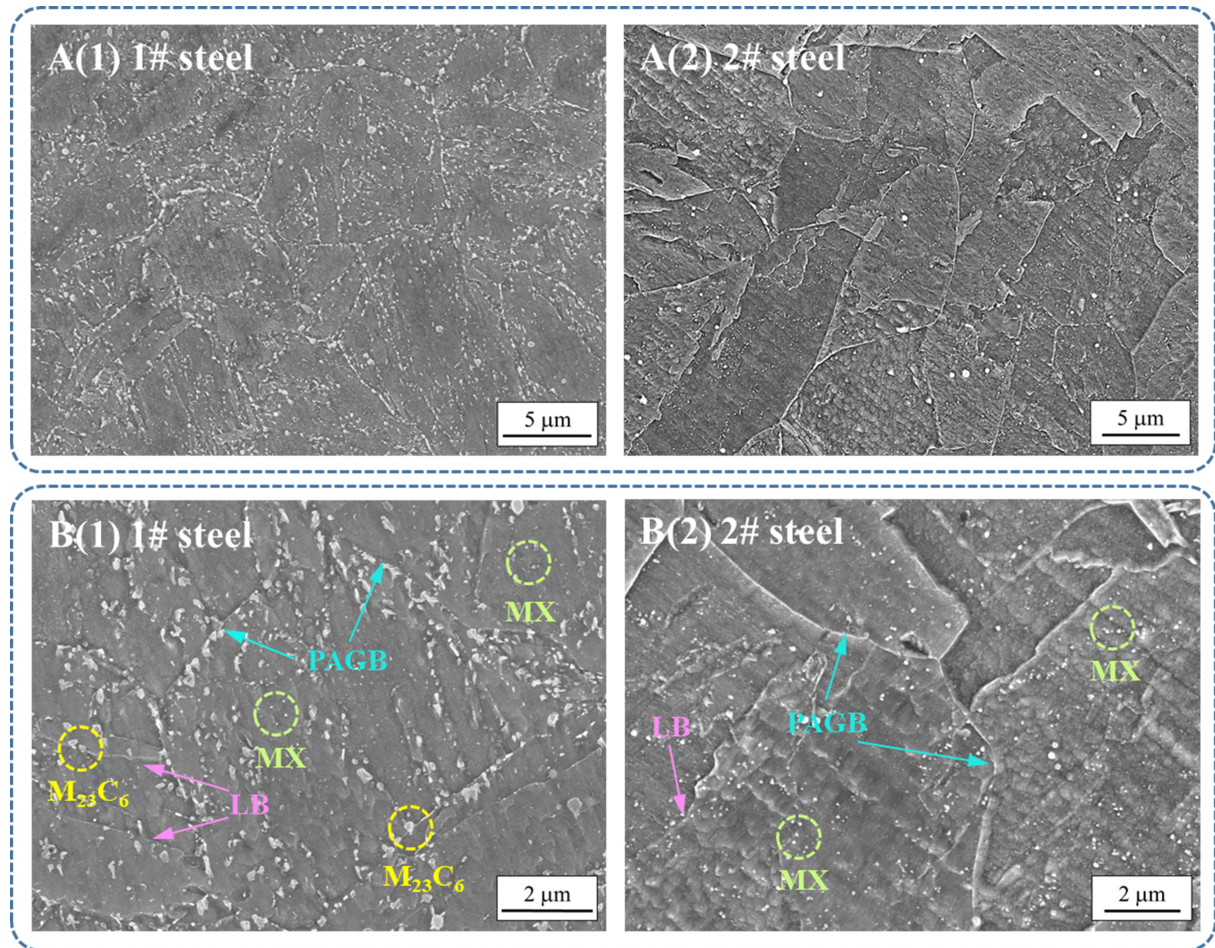
Figure 5. SEM micrographs of the designed RAFM steels: [A(1) and B(1)] 1# steel and [A(2) and B(2)] 2# steel. SEM: Scanning electron microscopy; RAFM: reduced activation ferritic-martensitic.

predictions from ML and CALPHAD.

The typical TEM micrographs of 1# and 2# steels are shown in Figure 6. As seen in Figure 6A(1) and B(1), the martensitic lath structures in both steels are decorated by dislocations and small precipitates. The lath width and dislocation density of 1# steel were measured to be around 334 nm and 2×10^{14} m^{-2}, respectively, whereas 2# exhibits a narrower lath width of 317 nm and a higher dislocation density of 3×10^{14} m^{-2}. As in conventional RAFM steels[47,48], the main precipitates observed in 1# steel are $M_{23}C_6$ and MX, as shown in Figure 6A(2) and (3). $M_{23}C_6$ precipitates have an average size of 48.4 nm and a number density of 2.32×10^{20} m^{-3}, primarily forming along PAGBs, sub-grain boundaries, and within martensitic laths. MX precipitates with an average size of 24.2 nm and a number density of 6.57×10^{20} m^{-3} are randomly distributed in the matrix. In 2# steel [Figure 6B(2) and (3)], only a large amount of MX precipitates randomly distributed in the matrix are observed, measuring 22.5 nm and 7.04×10^{20} m^{-3} in average size and number density, respectively.

The experimental measurement value for V_{M23C6} in 1# steel is about 1.38%, nearly matching the CALPHAD calculation of 1.30% and the ML prediction of 1.41%. Based on the experimental analysis results, the statistical V_{MX} of 1# steel is around 0.49%, which is less than the 0.6% calculated by CALPHAD and the
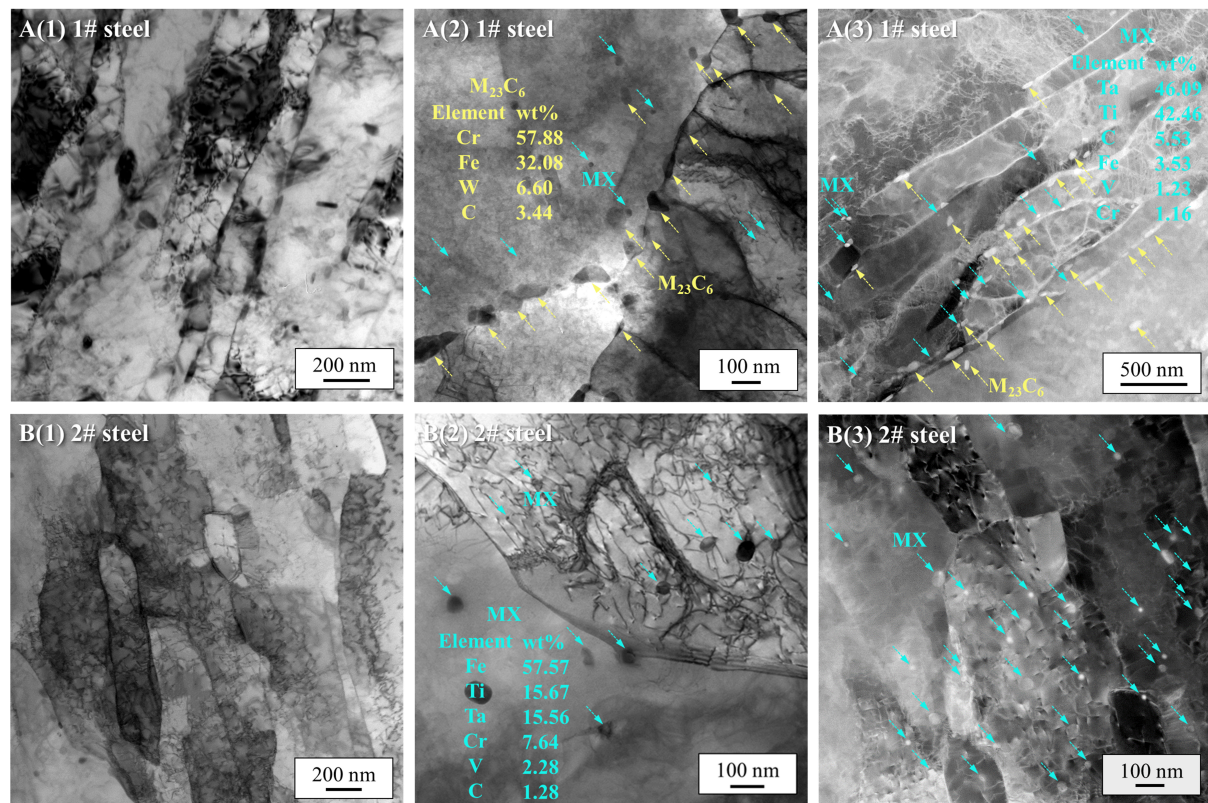
Figure 6. Typical TEM images of the designed RAFM steels: [A(1)-(3)] 1# steel and [B(1)-(3)] 2# steel. TEM: Transmission electron microscopy; RAFM: reduced activation ferritic-martensitic.

0.52% predicted by ML. This difference may arise from variable distributions of MX precipitates in different regions. Additionally, the possible presence of complex Ta/Ti-bearing oxides in 1# steel, similar to those found in CNA1[49], can reduce the amount of Ta/Ti available for forming MX precipitates, resulting in a lower experimental V_{MX} compared to calculated values. Similarly, the measured V_{MX} in 2# steel is 0.42%, which is lower than the predicted results from CALPHAD (0.50%) and ML (0.48%). Although the measured V_{MX} in both 1# and 2# steels is lower than the values predicted by CALPHAD and ML, it still meets our design requirement of ≥ 0.4%. The predictions concerning the microstructural attributes of δ-ferrite, coarsening phases, and V_{M23C6} are relatively accurate, confirming the reliability of our microstructural model.

The tensile tests of the prepared 1# and 2# steels were conducted at 25-600 °C, with their engineering stress-strain curves shown in Figure 7A and B. Table 2 summarizes the measured tensile properties of 1# and 2# steels at 600 °C. For 1# steel, the UTS reaches 404 MPa and the TE is 21.0%, meeting the specific design targets of UTS ≥ 400 MPa and TE ≥ 20%. For 2# steel, although the UTS of 422 MPa meets the strength requirement, the TE of 19.3% is slightly lower than the target of 20%. However, the difference of 0.7% from the targeted TE is considered acceptable for material design. As shown in Figure 7C and D, the tensile properties of 1# and 2# steels are compared to those of the conventional RAFM steels (i.e., Eurofer97[1,50], CLAM[51], JLF-1[52] and F82H[53]). The results indicate that both 1# and 2# steels exhibit higher UTS at the test temperatures of 25-600 °C, while their TE remains comparable to that of the conventional RAFM steels. Significantly, the UTS of 1# and 2# steels at 600 °C is ~100 MPa higher than that of the conventional RAFM steels, highlighting their superior tensile strength at elevated temperatures.
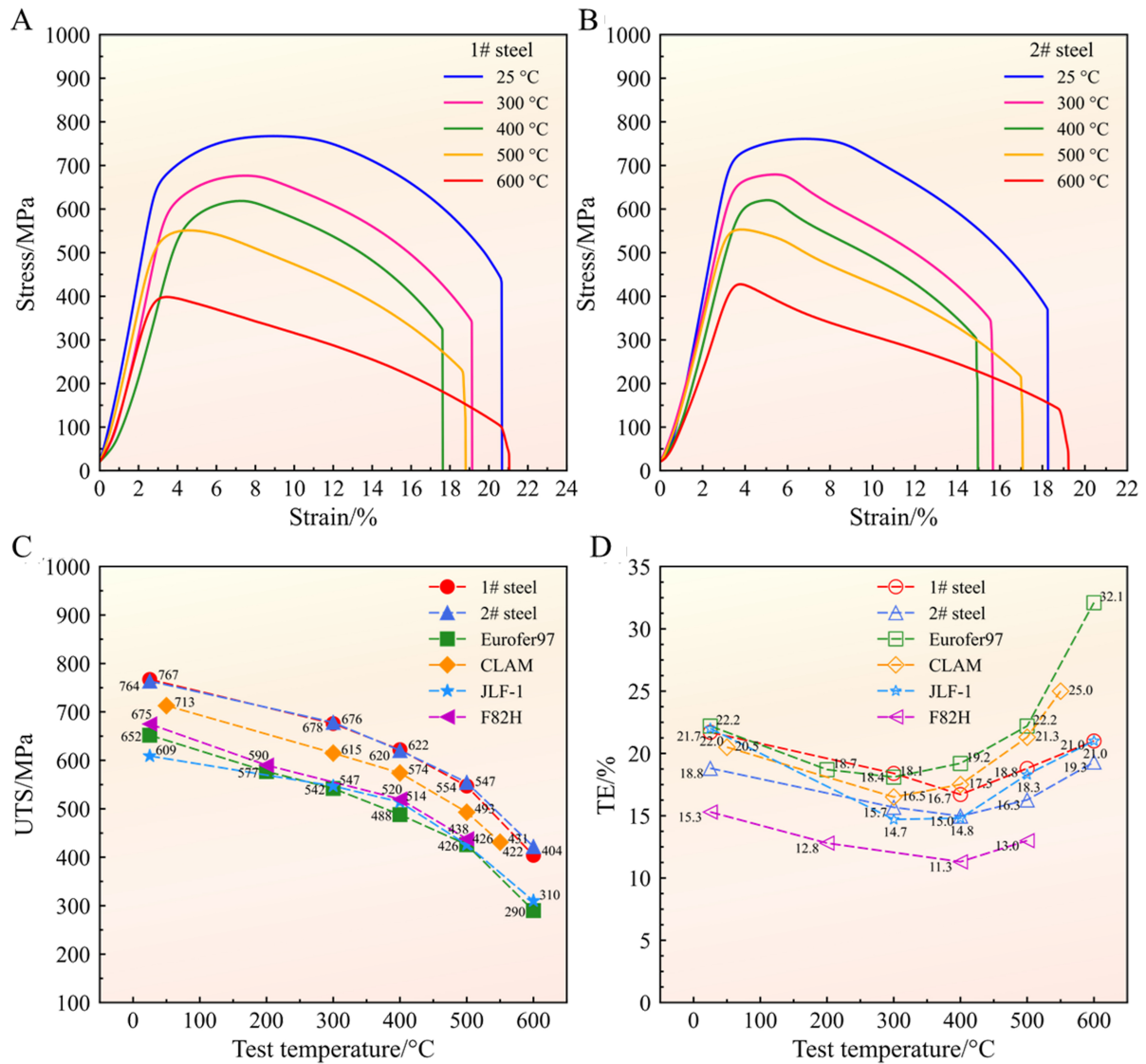
Figure 7. Stress-strain curves of RAFM steels at 25-600 °C: (A) 1# steel and (B) 2# steel; temperature-dependent tensile properties of 1# and 2# steels compared with literature data of Eurofer97[1,50], CLAM[51], JLF-1[52] and F82H[53]: (C) UTS and (D) TE. RAFM: Reduced activation ferritic-martensitic; Eurofer97: European RAFM steel; CLAM: China low activation martensitic; JLF-1: Japanese low activation Fe–9Cr–2WVTa; F82H: Japanese low activation ferritic 8Cr–2WVTa steel; UTS: ultimate tensile strength; TE: total elongation.

In summary, the integrated design model has effectively guided the design of novel RAFM steels with targeted microstructures and tensile properties, as evidenced by experimental results. SEM and TEM analyses confirm that the microstructures of 1# and 2# steels prepared in our laboratory meet the design goals, exhibiting a fully martensitic structure without δ-ferrite, Laves, and Z-phase. Both V_{MX} and V_{M23C6} in 1# and 2# steels also meet the specific structure requirements. Tensile testing at 600 °C indicates that 1# steel meets all performance criteria, while 2# steel meets the strength requirement but has a TE 0.7% below the target, which is still acceptable for material design. These results validate the effectiveness of the integrated design model for optimizing the compositions and processing conditions of RAFM steels to achieve targeted microstructures and tensile properties.

Discussion

The strengthening mechanisms of RAFM steels primarily include boundary strengthening ($\Delta\sigma_{bs}$), solid solution strengthening ($\Delta\sigma_{ss}$), dislocation strengthening ($\Delta\sigma_{ds}$), and precipitation strengthening from both MX-type ($\Delta\sigma_{ps-MX}$) and $M_{23}C_6$-type precipitates ($\Delta\sigma_{ps-M23C6}$), which are calculated by[48,54-57]:

$$\Delta\sigma_{bs} = k_{h\text{-}p}\, d_{pa}^{-\frac{1}{2}} \tag{5}$$

$$\Delta\sigma_{ss} = \sum k_i C_i^z \tag{6}$$

$$\Delta\sigma_{ds} = 0.25\, MGb\sqrt{\rho} \tag{7}$$

$$\Delta\sigma_{ps\text{-}MX} = \frac{0.7\, MGb\sqrt{V_{MX}}}{d_{MX}} \tag{8}$$

$$\Delta\sigma_{ps\text{-}M23C6} = M\alpha Gb\sqrt{N_{M23C6}\, d_{M23C6}} \tag{9}$$

where $k_{h\text{-}p}$ is a constant (0.62 MN$^{-1.5}$)[58]; d_{pa} is the average size of prior austenite grains; the hardening constant k_i for the main solute atoms W and Cr are 75.79 MPa at.%$^{-3/4}$ and 9.95 MPa at.%$^{-3/4}$, respectively[54]; C_i is the atomic fraction of element i (i.e., W or Cr); the exponent z is $3/4$ for substitutional solid solution[59]; M is the Taylor factor (3)[60]; G is the shear modulus (84 GPa)[61]; b is the Burgers vector (2.5×10^{-10} m)[60]; ρ is the dislocation density; d_{MX} and d_{M23C6} are the average sizes of MX and $M_{23}C_6$ precipitates, respectively; α is strength factor [$\alpha \approx 0.1757\, ln(2.7013 d_{M23C6})$][62]; and N_{M23C6} is the number density of $M_{23}C_6$ precipitates.

Table 3 summarizes the microstructural features of 1# and 2# steels, together with literature data of the conventional RAFM steels[6,20,21,27,51,63-66]. The strengthening contributions at room temperature, calculated by Equations (5)-(9), are also included in Table 3. The comparison between 1# and 2# steels and conventional RAFM steels indicates that:

i. Compared to 2# steel, 1# steel has a larger grain size but a higher solute atom concentration, leading to enhanced $\Delta\sigma_{ss}$. In contrast, 2# steel exhibits finer grains and achieves the higher $\Delta\sigma_{bs}$. The conventional RAFM steels show intermediate values for both aspects.

ii. Compared to other strengthening contributions, dislocations exhibit the highest strengthening effect in 1#, 2#, and conventional RAFM steels. The higher dislocation density in 2# steel (3×10^{14} m^{-2}) raises its $\Delta\sigma_{ds}$ to 272 MPa, compared to 223 MPa in 1# and conventional RAFM steels with dislocation density of 2×10^{14} m^{-2}.

iii. For 1# and 2# steels, the particle sizes of MX precipitates are 24.2 and 22.5 nm, with calculated V_{MX} of 0.49% and 0.42%, respectively. Consequently, 1# and 2# steels exhibit $\Delta\sigma_{ps\text{-}MX}$ of 128 and 127 MPa, respectively, which are ~70-110 MPa higher than those of conventional RAFM steels.

iv. The $M_{23}C_6$ precipitates in 1# steel have a size of 48.4 nm and a number density of 2.32×10^{20} m^{-3}, contributing to a $\Delta\sigma_{ps\text{-}M23C6}$ of 180 MPa, which is higher than ~98-154 MPa calculated in conventional RAFM steels.

The above analysis indicates that compared to conventional RAFM steels, the superior room-temperature strength of 1# steel primarily stems from increased $\Delta\sigma_{ps\text{-}MX}$ and $\Delta\sigma_{ps\text{-}M23C6}$. For 2# steel, its enhanced room-temperature performance is primarily driven by the improvement of $\Delta\sigma_{bs}$, $\Delta\sigma_{ds}$, and $\Delta\sigma_{ps\text{-}MX}$. At elevated temperatures, the strengthening effects from grain boundaries, dislocations, and $M_{23}C_6$ decrease significantly, while the nanoscale MX precipitates with excellent thermal stability can exert effective pinning

Table 3. Comparison of microstructural features and calculated strengthening contributions at room temperature for 1#, 2#, and conventional RAFM steels

Microstructural parameters		1#	2#	Conventional RAFM[6,20,21,27,51,63-66]
Prior austenite grains	Size (m)	18.8	9.7	~10-60
	$\Delta\sigma_{bs}$ (MPa)	143	199	~80-196
Solute atoms	W, Cr (at.%)	0.393, 9.234	0.078, 8.954	~0.3-0.6, ~8.5-9.8
	$\Delta\sigma_{ss}$ (MPa)	90	63	~80-107
Dislocations	Density (m^{-2})	2×10^{14}	3×10^{14}	~2×10^{14}
	$\Delta\sigma_{ds}$ (MPa)	223	272	~223
MX	Size (nm)	24.2	22.5	~15-30
	Density (m^{-3})	6.57×10^{20}	7.04×10^{20}	~10^{19}-10^{20}
	V_{MX} (%)	0.49	0.42	~0.002-0.15
	$\Delta\sigma_{ps-MX}$ (MPa)	128	127	~12-55
M$_{23}$C$_6$	Size (nm)	48.4	-	~70-200
	Density (m^{-3})	2.32×10^{20}	-	10^{19}-10^{20}
	$\Delta\sigma_{ps-M23C6}$ (MPa)	180		~98-154

RAFM: Reduced activation ferritic-martensitic.

effects. Therefore, the excellent high-temperature tensile properties of 1# and 2# steels are mainly related to the improved strengthening effect of MX precipitations. Moreover, according to previous studies[21,67-69], the 1# and 2# steels with high V_{MX} can exhibit excellent creep resistance. To further evaluate their suitability for fusion environments, long-term creep tests under various stress levels, temperature gradients, and environmental conditions are recommended. A more comprehensive creep constitutive model will also be developed to better predict material behavior and support the life assessment of fusion reactor structural materials.

CONCLUSIONS

In this study, a new design strategy was presented to develop RAFM steels with targeted microstructures and tensile properties using ML and CALPHAD methods. This strategy centers on utilizing microstructural and forward models to screen compositions and processing parameters suggested by the inverse model, meeting specific structure and performance criteria.

The key microstructural model, consisting of four sub-models, was developed to predict microstructural attributes based on CALPHAD data. It achieved an accuracy of >85% in predicting the presence of δ-ferrite and coarsening phases (i.e., Laves and Z-phase), and R^2 of > 0.9 for predicting V_{MX} and V_{M23C6}. Validated by CALPHAD and experiments, this microstructural model demonstrates strong reliability in guiding the microstructural optimization of RAFM steels.

An integrated design model was developed by combining the microstructural model with forward and reverse models, optimizing the compositions and processing for desired microstructures and tensile properties. Using this model, two novel RAFM steels with high V_{MX} and excellent tensile properties were designed and experimentally analyzed. In both steels, no δ-ferrite, Laves, and Z-phase were observed, and the V_{MX} (0.49%, 0.42%) and V_{M23C6} (1.38%, 0%) met the structure requirements. Tensile testing at 600 °C revealed a ~100 MPa increase in UTS compared to conventional RAFM steels. These experimental results are almost consistent with the targeted microstructures and tensile properties, confirming the effectiveness of our design strategy.

While this study has developed two new RAFM steels with high V_{MX} and excellent tensile properties, further investigations into long-term creep, irradiation, and corrosion resistance are required to fully assess their applicability under fusion conditions. Future research should focus on refining the integrated design model to accommodate complex service environments. Beyond developing high-performance RAFM steels, this model shows potential for application in the design of other advanced materials.

DECLARATIONS

Authors' contributions
Conceptualization, methodology, software, data curation, visualization, writing-original draft preparation: Li X
Writing-review and editing, supervision, project administration, funding acquisition: Zheng M
Investigation, discussion: Pan H, Mao C
Writing-review and editing, funding acquisition: Ding W

Availability of data and materials
The data and algorithms used in the current study will be available from the corresponding author based on reasonable request.

Conflicts of interest
All authors declared that there are no conflicts of interest.

Ethical approval and consent to participate
Not applicable.

Consent for publication
Not applicable.

Copyright

REFERENCES

1. Lindau R, Möslang A, Rieth M, et al. Present development status of EUROFER and ODS-EUROFER for application in blanket concepts. *Fusion Eng Des* 2005;75-9:989-96. DOI
2. Chun Y, Kang S, Lee D, et al. Development of Zr-containing advanced reduced-activation alloy (ARAA) as structural material for fusion reactors. *Fusion Eng Des* 2016;109-11:629-33. DOI
3. Raole PM, Deshpande SP; DEMO Team. Structural materials for fusion reactors. *Trans Indian Inst Met* 2009;62:105-11. DOI
4. Zinkle SJ, Busby JT. Structural materials for fission & fusion energy. *Mater Today* 2009;12:12-9. DOI
5. Aubert P, Tavassoli F, Rieth M, Diegele E, Poitevin Y. Review of candidate welding processes of RAFM steels for ITER test blanket modules and DEMO. *J Nucl Mater* 2011;417:43-50. DOI
6. Kano S, Yang H, Suzue R, et al. Precipitation of carbides in F82H steels and its impact on mechanical strength. *Nucl Mater Energy*

2016;9:331-7. DOI

7.   Mao C, Liu C, Yu L, Li H, Liu Y. Mechanical properties and tensile deformation behavior of a reduced activated ferritic-martensitic (RAFM) steel at elevated temperatures. *Mater Sci Eng A* 2018;725:283-9. DOI

8.   Rowcliffe A, Garrison L, Yamamoto Y, Tan L, Katoh Y. Materials challenges for the fusion nuclear science facility. *Fusion Eng Des* 2018;135:290-301. DOI

9.   Rowcliffe A, Kessel C, Katoh Y, et al. Materials-engineering challenges for the fusion core and lifetime components of the fusion nuclear science facility. *Nucl Mater Energy* 2018;16:82-7. DOI

10.   Cao H, Chen W. Effect of austenitizing temperature on microstructure and mechanical properties evaluation of microalloyed low-carbon RAFM steel. *Fusion Eng Des* 2023;190:113645. DOI

11.   Nagasaka T, Sakasegawa H, Tanigawa H, et al. Tensile properties of F82H steel after aging at 400-650 °C for 100,000 h. *Fusion Eng Des* 2015;98-9:2046-9. DOI

12.   Li Y, Nagasaka T, Muroga T, Huang Q, Wu Y. Effect of thermal ageing on tensile and creep properties of JLF-1 and CLAM steels. *J Nucl Mater* 2009;386-8:495-8. DOI

13.   Zhong B, Huang B, Li C, et al. Creep deformation and rupture behavior of CLAM steel at 823 K and 873 K. *J Nucl Mater* 2014;455:640-4. DOI

14.   Sawada K, Kushima H, Tabuchi M, Kimura K. Microstructural degradation of Gr.91 steel during creep under low stress. *Mater Sci Eng A* 2011;528:5511-8. DOI

15.   Mitsuhara M, Yamasaki S, Miake M, et al. Creep strengthening by lath boundaries in 9Cr ferritic heat-resistant steel. *Phil Mag Lett* 2016;96:76-83. DOI

16.   Xiao X, Liu G, Hu B, Wang J, Ma W. Coarsening behavior for $M_{23}C_6$ carbide in 12 %Cr-reduced activation ferrite/martensite steel: experimental study combined with DICTRA simulation. *J Mater Sci* 2013;48:5410-9. DOI

17.   Xu Y, Zhang X, Tian Y, et al. Study on the nucleation and growth of $M_{23}C_6$ carbides in a 10% Cr martensite ferritic steel after long-term aging. *Mater Charact* 2016;111:122-7. DOI

18.   Tan L, Byun T, Katoh Y, Snead L. Stability of MX-type strengthening nanoprecipitates in ferritic steels under thermal aging, stress and ion irradiation. *Acta Mater* 2014;71:11-9. DOI

19.   Chen J, Liu C, Wei C, Liu Y, Li H. Effects of isothermal aging on microstructure and mechanical property of low-carbon RAFM steel. *Acta Metall Sin* 2019;32:1151-60. DOI

20.   Xia Z, Zhang C, Yang Z. Control of precipitation behavior in reduced activation steels by intermediate heat treatment. *Mater Sci Eng A* 2011;528:6764-8. DOI

21.   Tan L, Snead L, Katoh Y. Development of new generation reduced activation ferritic-martensitic steels for advanced fusion reactors. *J Nucl Mater* 2016;478:42-9. DOI

22.   Kim T, Kim T, Cho Y, et al. Influence of Ti addition on MX precipitation and creep-fatigue properties of RAFM steel for nuclear fusion reactor. *J Nucl Mater* 2022;571:154001. DOI

23.   Mao C, Liu C, Yu L, Liu Y. Developing of containing Ta, Zr reduced activation ferritic/martensitic (RAFM) steel with excellent creep property. *Mater Sci Eng A* 2022;851:143625. DOI

24.   Jun S, Kim T, Im S, et al. Atomic scale identification of nano-sized precipitates of Ta/Ti-added RAFM steel and its superior creep strength. *Mater Charact* 2020;169:110596. DOI

25.   Zhou J, Shen Y, Xue W, Jia N, Misra R. Improving strength and ductility of low activation martensitic (LAM) steel by alloying with titanium and tempering. *Mater Sci Eng A* 2021;799:140152. DOI

26.   Klueh R. Reduced-activation steels: future development for improved creep strength. *J Nucl Mater* 2008;378:159-66. DOI

27.   Tan L, Katoh Y, Snead L. Development of castable nanostructured alloys as a new generation RAFM steels. *J Nucl Mater* 2018;511:598-604. DOI

28.   Yuan R, Liu Z, Balachandran PV, et al. Accelerated discovery of large electrostrains in $BaTiO_3$-based piezoelectrics using active learning. *Adv Mater* 2018;30:1702884. DOI

29.   Wen C, Zhang Y, Wang C, et al. Machine learning assisted design of high entropy alloys with desired property. *Acta Mater* 2019;170:109-17. DOI

30.   Yu J, Wang C, Chen Y, Wang C, Liu X. Accelerated design of L12-strengthened Co-base superalloys based on machine learning of experimental data. *Mater Design* 2020;195:108996. DOI

31.   Wang C, Shen C, Cui Q, Zhang C, Xu W. Tensile property prediction by feature engineering guided machine learning in reduced activation ferritic/martensitic steels. *J Nucl Mater* 2020;529:151823. DOI

32.   Li X, Zheng M, Yang X, Chen P, Ding W. A property-oriented design strategy of high-strength ductile RAFM steels based on machine learning. *Mater Sci Eng A* 2022;840:142891. DOI

33.   Andersson J, Helander T, Höglund L, Shi P, Sundman B. Thermo-Calc & DICTRA, computational tools for materials science. *Calphad* 2002;26:273-312. DOI

34.   Xiong J, Shi S, Zhang T. Machine learning of phases and mechanical properties in complex concentrated alloys. *J Mater Sci Technol* 2021;87:133-42. DOI

35.   Bobbili R, Ramakrishna B. Prediction of phases in high entropy alloys using machine learning. *Mater Today Commun* 2023;36:106674. DOI

36.   Chicco D, Warrens MJ, Jurman G. The coefficient of determination R-squared is more informative than SMAPE, MAE, MAPE, MSE

and RMSE in regression analysis evaluation. *PeerJ Comput Sci* 2021;7:e623. DOI PubMed PMC

37. Liu W, Wang C, Liang C, et al. Optimal design of γ'-strengthened high-entropy alloys via machine learning multilayer structural model. *Mater Sci Eng A* 2023;871:144852. DOI

38. Gholamy A, Kreinovich V, Kosheleva O. Why 70/30 or 80/20 relation between training and testing sets: a pedagogical explanation. *Int J Intell Technol Appl Stat* 2018;11:105-11. DOI

39. Rojas D, Garcia J, Prat O, et al. Effect of processing parameters on the evolution of dislocation density and sub-grain size of a 12%Cr heat resistant steel during creep at 650°C. *Mater Sci Eng A* 2011;528:1372-81. DOI

40. Pešička J, Kužel R, Dronhofer A, Eggeler G. The evolution of dislocation density during heat treatment and creep of tempered martensite ferritic steels. *Acta Mater* 2003;51:4847-62. DOI

41. Moon J, Lee C, Lee T, Jang M, Park M, Han HN. Phase transformation and impact properties in the experimentally simulated weld heat-affected zone of a reduced activation ferritic/martensitic steel. *J Nucl Mater* 2014;455:81-5. DOI

42. Yang L, Zhao F, Ding W. Laves phase evolution in china low-activation martensitic (CLAM) steel during long-term aging at 550 °C. *Materials* 2019;13:154. DOI PubMed PMC

43. Zhang X, Wu X, Liu R, Liu J, Yao M. Influence of Laves phase on creep strength of modified 9Cr-1Mo steel. *Mater Sci Eng A* 2017;706:279-86. DOI

44. Jiang L, Wang C, Fu H, Shen J, Zhang Z, Xie J. Discovery of aluminum alloys with ultra-strength and high-toughness via a property-oriented design strategy. *J Mater Sci Technol* 2022;98:33-43. DOI

45. Chen S, Rong L. Effect of silicon on the microstructure and mechanical properties of reduced activation ferritic/martensitic steel. *J Nucl Mater* 2015;459:13-9. DOI

46. Kim HK, Lee JW, Moon J, Lee CH, Hong HU. Effects of Ti and Ta addition on microstructure stability and tensile properties of reduced activation ferritic/martensitic steel for nuclear fusion reactors. *J Nucl Mater* 2018;500:327-36. DOI

47. Choi J, Moon J, Kim BH, et al. Tensile and Charpy impact properties of reduced activation ferritic/martensitic steel with small amounts of Ta and Ti. *J Nucl Mater* 2020;528:151862. DOI

48. Zhou J, Shen Y, Hong Y, Xue W, Misra R. Strengthening a fine-grained low activation martensitic steel by nanosized carbides. *Mater Sci Eng A* 2020;769:138471. DOI

49. Tan L, Yang Y, Busby J. Effects of alloying elements and thermomechanical treatment on 9Cr reduced activation ferritic–martensitic (RAFM) steels. *J Nucl Mater* 2013;442:S13-7. DOI

50. Terentyev D, Puype A, Kachko O, Van Renterghem W, Henry J. Development of RAFM steel for nuclear applications with reduced manganese, silicon and carbon content. *Nucl Mater Energy* 2021;29:101070. DOI

51. Huang Q. Status and improvement of CLAM for nuclear application. *Nucl Fusion* 2017;57:086042. DOI

52. Kasada R, Ono H, Sakesegawa H, Hirose T, Kimura A, Kohyama A. Mechanical properties of JLF-1 reduced-activation ferritic steels. *Fusion Sci Technol* 2003;44:145-9. DOI

53. Sakasegawa H, Tanigawa H. Mechanical properties of F82H plates with different thicknesses. *Fusion Eng Design* 2016;109-11:1724-7. DOI

54. Mao C, Liu C, Yu L, Li H, Liu Y. The correlation among microstructural parameter and dynamic strain aging (DSA) in influencing the mechanical properties of a reduced activated ferritic-martensitic (RAFM) steel. *Mater Sci Eng A* 2019;739:90-8. DOI

55. Taylor GI. The mechanism of plastic deformation of crystals. Part I. - Theoretical. *Proc R Soc Lond A* 1934;145:362-87. DOI

56. Lucas G. The evolution of mechanical property change in irradiated austenitic stainless steels. *J Nucl Mater* 1993;206:287-305. DOI

57. Cho KS, Park SS, Choi DH, Kwon H. Influence of Ti addition on the microstructure and mechanical properties of a 5% Cr–Mo–V steel. *J Alloys Compd* 2015;626:314-22. DOI

58. Li Y, Huang Q, Wu Y, Nagasaka T, Muroga T. Mechanical properties and microstructures of China low activation martensitic steel compared with JLF-1. *J Nucl Mater* 2007;367-70:117-21. DOI

59. Susila P, Sturm D, Heilmaier M, Murty B, Subramanya Sarma V. Effect of yttria particle size on the microstructure and compression creep properties of nanostructured oxide dispersion strengthened ferritic (Fe–12Cr–2W–0.5Y$_2$O$_3$) alloy. *Mater Sci Eng A* 2011;528:4579-84. DOI

60. Ramar A, Schäublin R. Analysis of hardening limits of oxide dispersion strengthened steel. *J Nucl Mater* 2013;432:323-33. DOI

61. Tavassoli A, Rensman J, Schirra M, Shiba K. Materials design data for reduced activation martensitic steel type F82H. *Fusion Eng Des* 2002;61-2:617-28. DOI

62. Tan L, Busby J. Formulating the strength factor α for improved predictability of radiation hardening. *J Nucl Mater* 2015;465:724-30. DOI

63. Dethloff C, Gaganidze E, Aktaa J. Quantitative TEM analysis of precipitation and grain boundary segregation in neutron irradiated EUROFER 97. *J Nucl Mater* 2014;454:323-31. DOI

64. Klueh R, Alexander D, Sokolov M. Effect of rhenium and osmium on mechanical properties of a 9Cr–2W–0.25V–0.07Ta–0.1C steel. *J Nucl Mater* 2000;279:91-9. DOI

65. Tong Z, Dai Y. The microstructure and tensile properties of ferritic/martensitic steels T91, Eurofer-97 and F82H irradiated up to 20dpa in STIP-III. *J Nucl Mater* 2010;398:43-8. DOI

66. Tanigawa H, Shiba K, Sakasegawa H, Hirose T, Jitsukawa S. Technical issues related to the development of reduced-activation ferritic/martensitic steels as structural materials for a fusion blanket system. *Fusion Eng Des* 2011;86:2549-52. DOI

67. Vivas J, De-Castro D, Altstadt E, Houska M, San-Martín D, Capdevila C. Design and high temperature behavior of novel heat resistant

steels strengthened by high density of stable nanoprecipitates. *Mater Sci Eng A* 2020;793:139799. DOI

68. Duan X, Zhu L, Zhang X, Huo J, Ren L. Evolution of the second phases in the weld seams of 2.25Cr-Mo-0.25 V steel in different heat treatment states. *Int J Mater Res* 2024;115:244-55. DOI

69. Öhlin O, Siriki R, Chai G. Long-term creep behaviours and structural stabilities of austenitic heat-resistant stainless steels. *Mater High Temp* 2024;41:61-72. DOI